



**HAL**  
open science

## **Lateral diffusivity coefficients from the dynamics of a SF6 patch in a coastal environment**

M. Kersalé, Anne Petrenko, A. M. Doglioli, D. Nencioli, J. Bouffard, S. Blain, Frederic Diaz, Thierry Labasque, Bernard Queguiner, I. Dekeyser

### ► **To cite this version:**

M. Kersalé, Anne Petrenko, A. M. Doglioli, D. Nencioli, J. Bouffard, et al.. Lateral diffusivity coefficients from the dynamics of a SF6 patch in a coastal environment. *Journal of Marine Systems*, 2016, 153, pp.42-54. <10.1016/j.jmarsys.2015.09.003>. <insu-01205846>

**HAL Id: insu-01205846**

**<https://insu.hal.science/insu-01205846v1>**

Submitted on 28 Sep 2015

**HAL** is a multi-disciplinary open access archive for the deposit and dissemination of scientific research documents, whether they are published or not. The documents may come from teaching and research institutions in France or abroad, or from public or private research centers.

L'archive ouverte pluridisciplinaire **HAL**, est destinée au dépôt et à la diffusion de documents scientifiques de niveau recherche, publiés ou non, émanant des établissements d'enseignement et de recherche français ou étrangers, des laboratoires publics ou privés.



HAL Authorization

# Accepted Manuscript

Lateral diffusivity coefficients from the dynamics of a  $SF_6$  patch in a coastal environment

M. Kersalé, A.A. Petrenko, A.M. Doglioli, F. Nencioli, J. Bouffard, S. Blain, F. Diaz, T. Labasque, B. Queguiner, I. Dekeyser

PII: S0924-7963(15)00155-4  
DOI: doi: [10.1016/j.jmarsys.2015.09.003](https://doi.org/10.1016/j.jmarsys.2015.09.003)  
Reference: MARSYS 2735

To appear in: *Journal of Marine Systems*

Received date: 5 March 2015  
Revised date: 30 July 2015  
Accepted date: 14 September 2015



Please cite this article as: Kersalé, M., Petrenko, A.A., Doglioli, A.M., Nencioli, F., Bouffard, J., Blain, S., Diaz, F., Labasque, T., Queguiner, B., Dekeyser, I., Lateral diffusivity coefficients from the dynamics of a  $SF_6$  patch in a coastal environment, *Journal of Marine Systems* (2015), doi: [10.1016/j.jmarsys.2015.09.003](https://doi.org/10.1016/j.jmarsys.2015.09.003)

This is a PDF file of an unedited manuscript that has been accepted for publication. As a service to our customers we are providing this early version of the manuscript. The manuscript will undergo copyediting, typesetting, and review of the resulting proof before it is published in its final form. Please note that during the production process errors may be discovered which could affect the content, and all legal disclaimers that apply to the journal pertain.

## Lateral diffusivity coefficients from the dynamics of a $SF_6$ patch in a coastal environment.

M. Kersalé<sup>a,\*</sup>, A. A. Petrenko<sup>b,c</sup>, A. M. Doglioli<sup>b,c</sup>, F. Nencioli<sup>d</sup>, J. Bouffard<sup>e</sup>,  
S. Blain<sup>f,g</sup>, F. Diaz<sup>b,c</sup>, T. Labasque<sup>h</sup>, B. Queguiner<sup>b,c</sup>, I. Dekeyser<sup>b,c</sup>

<sup>a</sup>Laboratoire de Physique des Océans, UMR 6523 CNRS-Ifremer-IRD-UBO, Université de Bretagne Occidentale, Brest, France

<sup>b</sup>Aix Marseille Université, CNRS/INSU, IRD, MIO, UM 110, 13288 Marseille, France.

<sup>c</sup>Université de Toulon, CNRS/INSU, IRD, MIO, UM 110, 83957 La Garde, France.

<sup>d</sup>Plymouth Marine Laboratory, Prospect Place, The Hoe, Plymouth PL1 3DH, United Kingdom.

<sup>e</sup>RHEA for ESA/ESRIN, via Galileo Galilei 2, 00044 Frascati, Italy.

<sup>f</sup>Sorbonne Universités, UPMC Univ Paris 06, UMR7621, Laboratoire d'Océanographie Microbienne, Observatoire Océanologique, 66650 Banyuls/mer, France.

<sup>g</sup>CNRS, UMR7621, Laboratoire d'Océanographie Microbienne, Observatoire Océanologique, 66650 Banyuls/mer, France.

<sup>h</sup>Université de Rennes 1, Géosciences Rennes, UMR CNRS 6118, 35042 Rennes, France.

---

### Abstract

The dispersion of a patch of the tracer sulfur hexafluoride ( $SF_6$ ) is used to assess the lateral diffusivity in the coastal waters of the western part of the Gulf of Lion (GoL), northwestern Mediterranean Sea, during the Latex10 experiment (September 2010). Immediately after the release, the spreading of the patch is associated with a strong decrease of the  $SF_6$  concentrations due to the gas exchange from the ocean to the atmosphere. This has been accurately quantified, evidencing the impact of the strong wind conditions during the first days of this campaign. Few days after the release, as the atmospheric loss of  $SF_6$  decreased, lateral diffusivity coefficient at spatial scales of 10 km has been computed using two approaches. First, the evolution of the patch with time was combined with a diffusion-strain model to obtain estimates of the strain rate ( $\gamma=2.5 \cdot 10^{-6} \text{ s}^{-1}$ ) and of the lateral diffusivity coefficient ( $K_h=23.2 \text{ m}^2 \text{ s}^{-1}$ ). Second, a steady state model was applied, showing  $K_h$  values similar to the previous method after a period of adjustment between 2 and 4.5 days. This

---

\*Corresponding author

Email address: marion.kersale@univ-brest.fr (M. Kersalé)

implies that after such period, our computation of  $K_h$  becomes insensitive to the inclusion of further straining of the patch. Analysis of sea surface temperature satellite imagery shows the presence of a strong front in the study area. The front clearly affected the dynamics within the region and thus the temporal evolution of the patch. Our results are consistent with previous studies in open ocean and demonstrate the success and feasibility of those methods also under small-scale, rapidly-evolving dynamics typical of coastal environments.

*Keywords:* Lateral diffusivity coefficient,  $SF_6$  tracer, Lagrangian referential, Coastal area

*2014 MSC:* 00-01, 99-00

---

## 1. Introduction

One of the major challenges in the study of ocean dynamics and mixing lies in estimating the dispersion of particles by turbulent processes. To describe it, classic theoretical studies have introduced the eddy diffusion coefficient,  $K_h$ , which parametrizes the effects of small scale turbulence. This coefficient is analogous to the one in Fick's first law of diffusion; however, it is associated to the mixing induced by small turbulence, rather than to molecular diffusion. The early study of [1] has showed that  $K_h$  depends on the length scale of the parametrized turbulent processes, introducing the concept of scale-dependent dispersion. In the following years, this scale dependence was confirmed by several experiments at sea by [2, 3, 4].

$K_h$  is a key parameter for the turbulent closure schemes of both global and regional numerical models. The simplest closure schemes usually assume isotropic, constant horizontal eddy diffusivity; more complex ones are based on spatio-temporally varying  $K_h$ , which depends on the dynamical characteristics of the resolved large scale processes [e.g. 5, 6, 7]. The accurate tuning of the values of eddy diffusivity is a key aspect for numerical experiments, since they strongly control the dispersion of physical and biogeochemical tracers [8]. Thus, *in situ* estimates of  $K_h$  provide crucial information for improving the performance and accuracy of ocean models.

Within the last decade the number of quantitative estimates of the scale-dependent  $K_h$  from *in situ* observations have increased with technological advancements. However, such quantifications still represent an observational challenge due to the small dimensions and short duration associated with turbulent processes. Estimates of  $K_h$  can be obtained from Eulerian or Lagrangian approaches. Generally, Eulerian estimates are obtained from remote sensing analysis [9, 10], while Lagrangian studies have been developed to calculate this coefficient *in situ*. Lagrangian-based estimates of  $K_h$  can be derived from the trajectories of freely drifting instruments, like surface drifters and subsurface floats [11] (for a extensive overview of the methods, see [12]). Eddy dispersion coefficients derived from

these methods are characteristic of oceanic mesoscale processes (length scales of  $\sim 10$ -100 km). In the last years, advancements in drifter technology, have favored the development of Lagrangian studies specifically designed to investigate coastal dynamics at smaller temporal and spatial scales [e.g. 13, 14, 15].

35 Such studies have helped improving our understanding of the contribution of local and non-local processes in regulating relative dispersions at scales below the Rossby radius of deformation. Furthermore, the quantification of  $K_h$  at the submesoscale has been recently investigated by [16] using trajectories of hundreds of tracked surface drifters.

40 The determination of  $K_h$  associated with the smaller scales, has been usually developed from experiments based on inert tracers. Among various types of tracer, fluorescent dyes, especially Rhodamine B, have been largely used to study turbulent diffusion [17]. Although numerous dye experiments have also been performed in coastal environments or fresh water lakes, very few of these  
45 studies have been made in stratified coastal areas with strong mesoscale activity. Noteworthy exceptions include the rhodamine dye experiments in the Massachusetts Bay [18] and the Coastal Mixing and Optics (CMO) project [19]. Dye experiments have been also deployed in the stratified thermoclines of the Celtic Sea on the NW European Shelf by [20] and [21] and in the northern Monterey Bay, California by [22].

50 The sulfur hexafluoride ( $SF_6$ ), a stable and inert gas detectable at concentrations a million times lower than dyes, has been mainly used for open ocean tracer experiments. The main advantage of the  $SF_6$  is that, due to its low background concentration in seawater, it can be used via small injections of  $SF_6$  saturated  
55 seawater [23]. Nevertheless its low solubility in water makes it more difficult to inject than dye tracers. Since the mid 1980s,  $SF_6$  has been widely employed in horizontal turbulent processes studies. More recently  $CF_3SF_5$  (trifluoromethyl sulfur pentafluoride), with same properties and behavior, has emerged as a viable alternative to  $SF_6$  for large scale experiment [24, 25, 26]. Since the  
60 successful test release of  $CF_3SF_5$  had not yet been undertaken during the implementation of the project, we used  $SF_6$  rather than  $CF_3SF_5$ .

Lateral diffusivities at scales smaller than 100 km have been obtained during various  $SF_6$  tracer experiments (NATRE, [23] ; IronEx-I, [27] ; SOIREE, [28] ; PRIME, [29]). Such estimates are based on the hypothesis that, under local  
65 mesoscale stirring (which can be approximated, to a first order, as 2-dimensional and divergence-free), the initial shape of the tracer patch will elongate along one direction while thinning along the other. The width of the patch will keep decreasing until the effects of mesoscale stirring are balanced by smaller scale diffusion and an equilibrium is reached. Thus, lateral diffusivity can be com-  
70 puted by combining estimates of the strain rate with *in situ* measurements of the patch width. Strain rate is usually estimated from successive *in situ* mappings [23] or from the analysis of satellite imagery of surface tracers (*e.g.* chlorophyll-  
a concentration [28]). Lateral diffusivities computed using this approach range from 0.5 to 25  $m^2 s^{-1}$  for tracer filaments with widths between 1 and 10 km.

75 At similar scales but in lower energetic systems, lateral diffusivities have also been estimated (from  $SF_6$  in the Santa Monica Basin Tracer Experiment, [30] and from  $CF_3SF_5$  in the BATRE one, [26]) by neglecting the strain and measuring the growth of the roughly circular tracer patch. Following this method, the lateral diffusivities were of the order of 10  $m^2 s^{-1}$  for the interior of the two  
80 basins at scales on the order of 10 km.

Estimates of lateral diffusivity can be used to understand the dynamics and mixing within specific water patches, and therefore to assess the rates of some biogeochemical processes. In the case of biogeochemical applications,  $SF_6$  has been used to estimate deep-water ocean ventilation, pathways, and anthropogenic  
85  $CO_2$  uptake [31, 32, 33]. During the PRIME project (Plankton Reactivity In the Marine Environment), the evolution of an  $SF_6$  patch has allowed a quantitative understanding of the nutrient supply into the mixed layer of an anticyclonic eddy in the North Atlantic [29, 34]. Combined with iron enrichment, the  $SF_6$  tracer has provided the potential to assess ecosystem responses to added iron  
90 [35, 36, 37, 38, 39].

As mentioned before,  $SF_6$  has been rarely used in coastal areas, where the circulation is usually complex due to the influence of different forcings (local

atmospheric conditions, tides, freshwater inputs) and the constraints imposed on the flow by its coastline and bathymetry [40]. Coastal dynamics is critical for regulating the cross-shore exchange of materials between continents and oceans. The study of its functioning is therefore of considerable interest for understanding the coupling of terrestrial and oceanic biogeochemical cycles. Two  $SF_6$  experiment have been conducted in the Florida shelf [41] and near South Georgia [42]. Given the success of these first  $SF_6$  tracer experiments, our study explores the application of  $SF_6$  in a coastal area of the North Western Mediterranean Sea where several *in situ* data have been collected within the framework of the LATEX project (LAGrangian Transport EXperiment, 2007-2011 ; <http://www.mio.univ-amu.fr/LATEX>).

The LATEX project aimed to investigate the role of coupled physical and biogeochemical dynamics at the mesoscale in regulating the exchanges of matter and energy between inshore and offshore areas. One of the goals of the project was to analyze transport patterns and diffusion rates in the western part of the Gulf of Lion (GoL). The GoL is located in the northwestern Mediterranean Sea and is characterized by a relatively large continental margin (Fig. 1-a). Its hydrodynamics is complex and highly variable in space and time [43]. Its circulation is strongly influenced by the southwestward along-slope Northern Current (NC). This density current flows in a cyclonic way and constitutes an effective dynamical barrier isolating the coastal waters of the continental shelf from the open northwestern Mediterranean Sea [44, 45, 46]. Cross-shore exchanges between the GoL and offshore waters are mainly regulated by wind induced dynamics [47, 48], and by processes associated with the NC, such as intrusion into the continental shelf, barotropic and baroclinic instabilities arising along its internal and external borders and seasonal modulation of its intensity and position [49, 50, 51].

Two of the four LATEX field campaigns were dedicated to the  $SF_6$  tracer release experiment. The first one, the Latex00 campaign (9-11 June 2007, aboard the R/V Téthys II), was part of a pilot project that aimed to measure the background concentration of  $SF_6$  and to test the Lagrangian navigation software

[LATEXtools, 52]. The last one, the Latex10 campaign (1-24 September 2010,  
125 aboard the R/V Le Suroît and the R/V Téthys II), investigated the transport  
structures in the western GoL with an adaptive sampling strategy, which com-  
bined satellite data, ship-based ADCP measurements, and iterative Lagrangian  
drifter releases. The sampling strategy enabled the identification of a frontal  
jet, 10 km-wide, roughly parallel to the coast, along which waters from the  
130 continental shelf left the gulf towards the Catalan Basin [53].

The aim of the present work is to use the observations from the Latex10 pas-  
sive tracer experiment to evaluate the lateral diffusivity coefficient in a coastal  
area (between depths of 100 and 1000  $m$ ), marked by the presence of an ener-  
getic small scale dynamical feature. The methods to release and measure the  
135  $SF_6$  data are described in Section 2, while the analysis and evolution of the  
 $SF_6$  patch are showed in Section 3. Air-sea gas exchanges are described in Sec-  
tion 4. In Section 5, the different methods for calculating the lateral diffusivity  
coefficients, their limits and their applications in the GoL are presented. The  
estimated coefficients, the temporal evolution of the patch and the air-sea gas  
140 exchanges are discussed in Section 6.

## 2. SF<sub>6</sub> release and measurements

A saturated SF<sub>6</sub> solution was prepared at the beginning of the Latex10 campaign. A 7000 L steel tank was filled with sea water in the afternoon of September 2. An acrylic cylinder was placed on the top of the tank, making a headspace of about 5 L for effective bubbling. Pure SF<sub>6</sub> gas was injected into the seawater in the tank for 48 h to obtain a saturated SF<sub>6</sub> solution. For determining SF<sub>6</sub> concentrations in the tank before injection, a headspace extraction and a classical gas chromatograph (GC) equipped with a thermal conductivity detector (TCD) were used. The GC/TCD analysis of extracted gas were based on the [54] method. The measured SF<sub>6</sub> concentration was  $1.63 \cdot 10^{-4} \text{ mol L}^{-1}$  for the first 4000 L released. Due to a technical problem, the SF<sub>6</sub> concentration decreased to  $0.69 \cdot 10^{-4} \text{ mol L}^{-1}$  for the remaining 3000 L. Lateral and vertical homogeneities in the distribution within the area are still a primary assumption, with or without this technical problem. Such hypothesis was likely respected, since the analysis of the lateral diffusivity was performed after a period of 2 days after the release, as in [55].

In order to release the tracer as homogeneously as possible in the horizontal and, thus, study the lateral diffusivity of the tracer patch while minimizing the contribution due to the advection, it was necessary to coordinate the release of the SF<sub>6</sub> in a Lagrangian reference frame. This task was accomplished using the software package LATEXtools [52], that provided information to direct the ship route during the tracer release. The center of the Lagrangian reference frame was defined by the position of a buoy (which is hereafter referred to as the “reference buoy”) drogued at 11.5 m depth and deployed at 42°45,01’N - 3°30,11’E at the beginning of the tracer release on September 11 (Fig. 1-b). The reference buoy was equipped with an Iridium transmitter/receiver which ensured the acquisition of its position every 15 minutes. The position of the Lagrangian reference frame and, accordingly, the ship trajectory were adjusted after each acquisition. From the R/V Le Suroît, the saturated SF<sub>6</sub> solution was released at a ship speed of 4 knots for a period of 14 h (Table 1). The reconstructed vessel

track in the Lagrangian reference frame matched almost perfectly the planned route [See Figure 6 in 52]. Unfortunately, during the cruise the atmospheric conditions were particularly rough (wind gust exceeding  $30 \text{ m s}^{-1}$ , Fig. 5-a). In order to prevent as much as possible a quick loss and dispersion of the tracer, the location of the release has been chosen on the basis of the information coming from the weather-forecast model Aladin and a 10-year realistic simulation from a high-resolution ocean circulation model [56]. Indeed, we chose to release the  $SF_6$  during the predicted period of low winds (which indeed turned out to be lower than  $10 \text{ m s}^{-1}$ , Fig. 5-a) and at the point of current speed minimum as determined in the historical archive of our numerical simulations for similar dynamical and meteorological forcings.

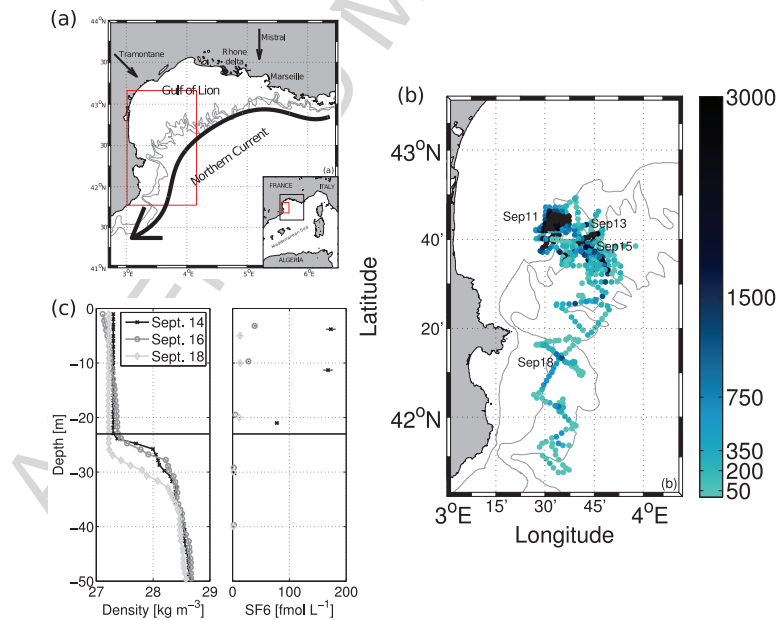


Figure 1: (a) Bathymetry of the Gulf of Lion (200 and 500 m isobaths). Black arrows indicates the Northern Current, and the Tramontane and Mistral winds. The red rectangle indicates the region of focus of the Latex10 campaign. (b) Map of the  $SF_6$  patch, color-coded by  $SF_6$  concentrations [ $\text{fmol L}^{-1}$ ] and marked on selected dates. Isobaths at 100, 200 and 1000 m are plotted with thin lines. (c) Vertical profiles of density [ $\text{kg m}^{-3}$ ] and  $SF_6$  concentrations [ $\text{fmol L}^{-1}$ ] on September 14, September 16 and September 18.

A  $SF_6$  background value of about  $1.35 \text{ fmol L}^{-1}$  ( $\text{fmol}=10^{-15} \text{ mol}$ ) was estimated during the Latex00 campaign. Such value was used as a reference to design the Latex10 release system and the sampling strategy. Further measurements performed during the Latex10 campaign confirmed that, although slightly  
185 higher, background  $SF_6$  concentrations at the time of the experiment were of the same order of magnitude (average equal to  $1.72 \text{ fmol L}^{-1}$ ). In total, 7000 L of  $SF_6$ -saturated seawater were released at 7 m depth inside a square area of  $\sim 30 \text{ km}^2$ . Based on the volume of injected seawater and the  $SF_6$  concentration inside the tank, the total quantity of  $SF_6$  initially released in the water has been  
190 estimated as  $0.89 \pm 0.12 \text{ mol}$ . Assuming a rapid vertical redistribution of  $SF_6$  inside the mixed layer, characterized by a depth of about 23 m on September 14 (Fig. 1-c), this release assured the formation of a patch with  $SF_6$  concentrations of about  $1250 \text{ fmol L}^{-1}$ , 727 times higher than the background value.

After the release, the horizontal evolution of the tracer patch was monitored  
195 for 7 days (Fig. 1-b) during a series of 4 successive horizontal mappings at 3 m depth (Table 1). The analytical system used for the measurements of  $SF_6$  was based on continuous flow purge and trap (PT) extraction followed by gas chromatography separation and detection by electron capture detector (GC/ECD ; See Appendix A for a detailed description). This system is different from the  
200 previous ones developed by [57] and [58], since it is not based on vacuum sparge sample extraction, but on continuous flow of purified nitrogen for extraction of dissolved gases. The samples were analyzed at a frequency of 6 samples per hour, analogous to previous studies [57]. The uncertainty has been estimated at 5 % for concentrations above the detection limit ( $0.8 \text{ fmol L}^{-1}$ ). Moreover,  
205 three profiles (six samples per profile) were performed at different stations to ensure the homogeneity of the mixed layer (Fig. 1-c). These profiles revealed a bottom depth of the mixed layer constant with space and time, between 23 and 26 m depth. Concentrations of  $SF_6$  in the mixed layer are reasonably homogeneous (Fig. 1-c). In the presence of a strong gradient, as it is the case at the  
210 bottom of the mixed layer depth, the error due to the low resolution of vertical sampling of  $SF_6$  (Niskin bottle) can explain an intermediate value as the one of

78  $\text{fmol L}^{-1}$  measured on September 14 at 21 m depth.

In our analysis, the surface  $SF_6$  concentration data have been re-mapped in a Lagrangian reference frame in which the origin moves with the center of mass  
 215 of the tracer [19]. The spatially irregular data along the ship track are interpolated onto a regular grid using natural neighbor interpolation. This local method, based on the Voronoi diagram [59, 60], has the advantage of accommodating the resolution to the spatial distribution of the initial scattered data.

Table 1: Start and end dates of the release and mapping of the tracer.

	Beginning		End		Time intervals
	Day	Hour (GMT)	Day	Hour (GMT)	
Release	Sept. 11	04h02	Sept. 11	18h00	14 h
Mapping 1	Sept. 11	22h11	Sept. 12	15h49	17.6 h
Mapping 2	Sept. 13	18h40	Sept. 14	12h50	18.2 h
Mapping 3	Sept. 15	18h17	Sept. 16	15h55	21.6 h
Mapping 4	Sept. 18	05h48	Sept. 18	22h03	16.2 h

In the remainder of the study, our analysis of the  $SF_6$  patch is based on the  
 220 advection-diffusion equation, governing the evolution of the Reynolds-averaged, passive tracer concentration  $C$  ( $\text{mol m}^{-3}$ ) in an incompressible fluid. Generally, it is based on the hypothesis of a two-dimensional linear strain field in which the strain rate ( $\gamma = \frac{\partial u}{\partial x} = -\frac{\partial v}{\partial y}$ ) varies with time but is homogeneous in space, and the horizontal diffusivity is constant and isotropic. It follows that, the  
 225 advection-diffusion equation can be written as:

$$\frac{\partial C}{\partial t} + \gamma x \frac{\partial C}{\partial x} - \gamma y \frac{\partial C}{\partial y} = K_h \left( \frac{\partial^2 C}{\partial x^2} + \frac{\partial^2 C}{\partial y^2} \right) + \frac{\partial}{\partial z} F \quad (1)$$

with  $F = K_z \frac{\partial C}{\partial z}$  is the vertical flux of tracer ( $\text{mol m}^{-2} \text{ s}^{-1}$ ), and  $K_h$  and  $K_z$  are the horizontal and vertical diffusivity coefficients ( $\text{m}^2 \text{ s}^{-1}$ ), respectively.

### 3. $SF_6$ evolution

To evaluate the extension of the patch, we have estimated the  $SF_6$  patch area  
 230 using two methods. Both are based on the hypothesis that, after the release,

$SF_6$  concentrations within the patches can be approximated by a Gaussian distribution [e.g. 28, 19, 39, 61].

Following [39], we performed a first estimate of the total area of the patch based on the contour lines concentrations of  $SF_6$ . We defined  $A_{CL}$  as the area inside the contour lines  $[SF_6]_{max}e^{-2}$ , with  $[SF_6]_{max}$  the maximum concentration of the *in situ* mapping. Thus, for an idealized Gaussian patch,  $A_{CL}$  represents the area where 95.4 % of the total concentration is present. The  $A_{CL}$  for the four mappings are shown in Fig. 2 (red lines).

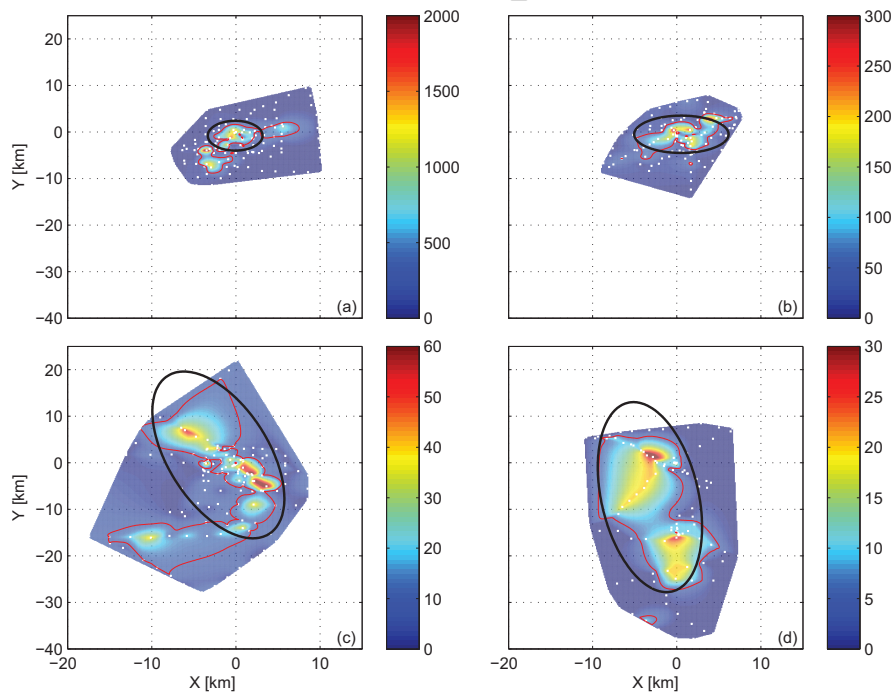


Figure 2: Lagrangian maps of  $SF_6$  concentration [ $\text{fmol L}^{-1}$ ] for Mapping 1 (a), Mapping 2 (b), Mapping 3 (c) and Mapping 4 (d). The plots are referenced to the position of the center mass. Note that the color bar maximum varies with each mapping. The  $[SF_6]_{max}e^{-2}$  contour lines are shown in red in each plot indicating the patch area with the contour line technique ( $A_{CL}$ ). Gaussian ellipsoids are shown in black in each plot indicating the fitting patch area ( $A_{GE}$ ). The locations of  $SF_6$  measurements are indicated by the white dots.

For the second method, Gaussian ellipsoids (black ellipsoids, Fig. 2) have been

240 fitted to the horizontal mapping of  $SF_6$  using an unconstrained non-linear optimization. The Gaussian ellipsoids fit are obtained by minimizing the function for each distribution, starting at an initial estimate and using the Optimization Toolbox routines, which are based on the Nelder-Mead simplex search algorithm [62]. The Gaussian ellipsoids fit can be sensitive to the initial estimate.

245 To better address this aspect, we have varied the initial estimates of the Gaussian ellipsoid, and hence the total number of fits. We have then calculated the averaged values and the standard deviations of the length of the major and minor axis, the center of the ellipse and the angle. With this technique, the area inside the Gaussian ellipsoid ( $A_{GE} = \pi\sigma_l\sigma_w$ ) can be used to calculate a second

250 estimate of the  $SF_6$  patch total area, with  $\sigma_l$  and  $\sigma_w$  the estimated lengths of the semi-major and the semi-minor axis of the  $SF_6$  patch area respectively. Successive estimates of the  $SF_6$  patch area based on the two techniques ( $A_{CL}$ ,  $A_{GE}$ ) are used to analyze the temporal evolution of its spreading (Fig. 3-a). The lengths of the two semi-axis of the patch for each mapping are represented

255 as a function of time in Fig. 3-b and listed in Table 2. For further characterizing the patch geometry, the perimeter of the Gaussian ellipsoid has been calculated with the common Ramanujan method:

$$P = \pi(3(\sigma_l + \sigma_w) - \sqrt{(3\sigma_l + \sigma_w)(\sigma_l + 3\sigma_w)}) \quad (2)$$

If the strain induced by the current remains constant and uniform, the aspect ratio of an initially circular patch, estimated as the ratio Area/Perimeter<sup>2</sup> and

260 scaled using a factor of  $4\pi$ , would start at 1 and decreases as the patch stretches into a filament. This ratio is represented in Fig. 3-c as a function of time.

We can identify two phases in the temporal evolution of the  $SF_6$  patch. Initially, between September 12 to September 14 (Mappings 1 and 2), the patch of tracer spreads slowly in both directions with a small increase of its length and

265 width. During this first phase, the area increases according to both methods: about  $38 \pm 2 \text{ km}^2$  for  $A_{GE}$  and  $6 \text{ km}^2$  for  $A_{CL}$  (no errors have been defined in the literature for this method). Within the same period, the  $SF_6$  concentrations decrease of one order of magnitude. Starting from September 14, the semi-major

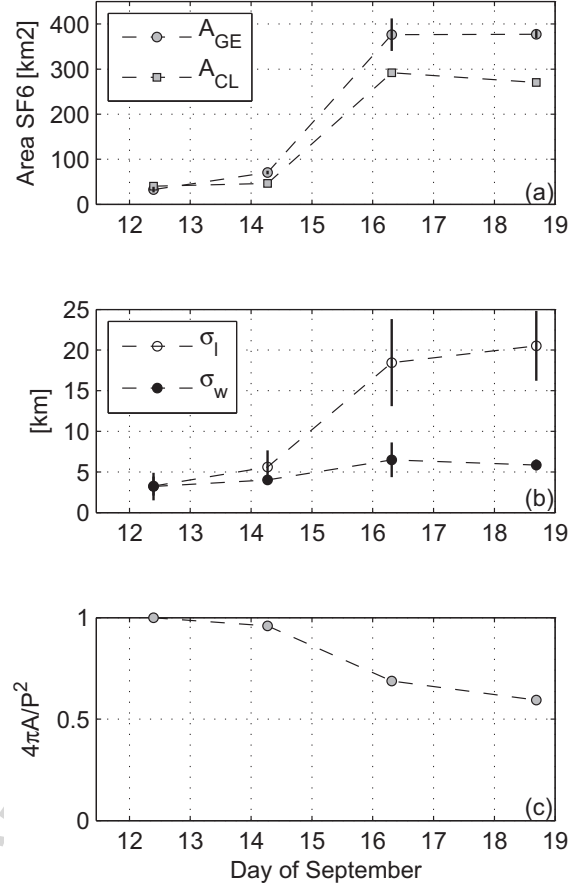


Figure 3: (a) Temporal evolution of the surface area [km<sup>2</sup>] of the patch estimated by Gaussian ellipsoids (gray circles -  $A_{GE}$ ) and  $[SF_6]_{max}e^{-2}$  contour lines (gray squares -  $A_{CL}$ ) fitted to the mapped  $SF_6$  data. (b) The lengths of the semi-major ( $\sigma_l$ , white circles) and semi-minor ( $\sigma_w$ , black circles) axis of the Gaussian ellipsoids fitted to the mapped  $SF_6$  data. (c) Aspect ratio of the patch total area ( $A_{GE}$ ) as  $area/(perimeter)^2$ . The ratio is normalized to 1 for an idealized circular patch by multiplying it by  $4\pi$ . The vertical black lines over the circles (a,b) represent the estimated uncertainties on the calculation of  $\sigma_l$  and  $\sigma_w$ . They are always calculated for the Gaussian ellipsoids calculations, and thus they are negligible when not visible.

axis of the patch ( $\sigma_l$ ) increases quickly, while the semi-minor axis ( $\sigma_w$ ) remains  
 270 approximately constant. During this second phase, the spreading of the patch is

Table 2: Estimates of the lengths of the semi-major axis and the semi-minor axis of the  $SF_6$  patch for each mapping.

	$\sigma_l$ (km)	$\sigma_w$ (km)
Mapping 1	$3.3 \pm 1.2$	$3.2 \pm 1.7$
Mapping 2	$5.6 \pm 2$	$4 \pm 0.6$
Mapping 3	$18.4 \pm 5.4$	$6.5 \pm 2.1$
Mapping 4	$20.5 \pm 4.3$	$5.9 \pm 0.7$

anisotropic, with  $\sigma_l$  as much as 3 times the length of  $\sigma_w$ . Strong area increases are observed by both estimates: between Mapping 2 and Mapping 3  $A_{GE}$  ( $A_{CL}$  respectively) increases from  $70 \pm 4$  (46)  $\text{km}^2$  to  $376 \pm 90$  (292)  $\text{km}^2$ , corresponding to an area increase of  $306 \pm 16$  (246)  $\text{km}^2$ , one order of magnitude larger than  
 275 during the first period. A decrease of the area to perimeter ratio (Fig. 3-c) is observed during both phases, indicating that the patch is progressively stretched into a filament.

Further evidence of this stretching event is obtained by superposing the *in situ*  $SF_6$  concentrations on AVHRR (Advanced Very High Resolution Radiometer)  
 280 channel 4 imagery provided by Météo-France (Fig. 4). AVHRR channel 4 measurements are usually inaccurate in estimating the absolute values of the sea surface temperature (SST). However, AVHRR channel 4 (hereafter pseudo-SST) imagery has shown to accurately identify the spatial distribution of SST gradients [*e.g.* 63]. Therefore, pseudo-SST can be successfully used to reconstruct  
 285 the dynamics of the waters surrounding the patch. On September 12, the tracer patch extends southwestward over the continental shelf, which is characterized by colder surface waters with pseudo-SST around  $16^\circ\text{C}$  (Fig. 4-a). After two days, a front between warmer waters from the Northern Current (pseudo-SST  $\sim 19^\circ\text{C}$ ) and colder waters from the shelf is formed along the western continental  
 290 slope of the gulf (at  $4^\circ\text{E}$  - Fig. 4-b). By that time, the tracer patch has slightly drifted eastward toward the western boundary of the front. The dynamical characteristics of the frontal structure detected during the Latex10 campaign have been fully described in the study of [63]. On September 15,

the contour line of the total patch area shows a distribution of the tracer elongated along a tongue of colder coastal waters (Fig. 4-c). On September 18, no  
 295 pseudo-SST satellite image was available due to cloud coverage, when the tracer is located in front of Cape Creus after a significant southward drift (Fig. 4-d). The analysis of pseudo-SST reveals that the second phase of evolution of  $SF_6$ , identified from Fig. 3, is associated with the intense stirring induced by the  
 300 dynamics of the strong thermal front.

#### 4. Air-sea gas exchange

Other than changes in area and geometry, the patch evolution included variations in  $SF_6$  maximum concentration due to air-sea gas exchange. The maximum concentration of  $SF_6$  decreases from  $3000 \pm 150$  fmol L<sup>-1</sup> on September 11  
 305 (Mapping 1), to  $50 \pm 2.5$  fmol L<sup>-1</sup> on September 18 (Mapping 4, Fig. 1-b). The  $SF_6$  is an inert tracer, and therefore its dynamics has no internal sources or sinks. To investigate the evolution of  $SF_6$  concentration within the mixed layer after its release, two vertical boundary conditions are required: one at the bottom of the mixed layer, and one at the ocean-atmosphere interface.  
 310 We can consider the exchanges that occur between the mixed layer and the underlying waters to be negligible since in late summer (the cruise took place in September) the GoL is characterized by a strong stratification. Thus, the flux at the bottom of the mixed layer (depth equal to  $-z_{mix}$ ) can be defined as:

$$F|_{z=-z_{mix}} = 0 \quad (3)$$

Regarding the second boundary condition, the flux of  $SF_6$  across the air-sea  
 315 interface (negative when the flux is from atmosphere to ocean) can be expressed as:

$$F|_{z=0} = k(C_w - \alpha C_a) \quad (4)$$

where  $k \equiv k(t)$  is the transfer velocity (m s<sup>-1</sup>, see details on its dependence on wind in subsection 4.1),  $C_w$  is the tracer concentration few cm below the water surface (mol m<sup>-3</sup>),  $C_a$  the tracer concentration in air just above the

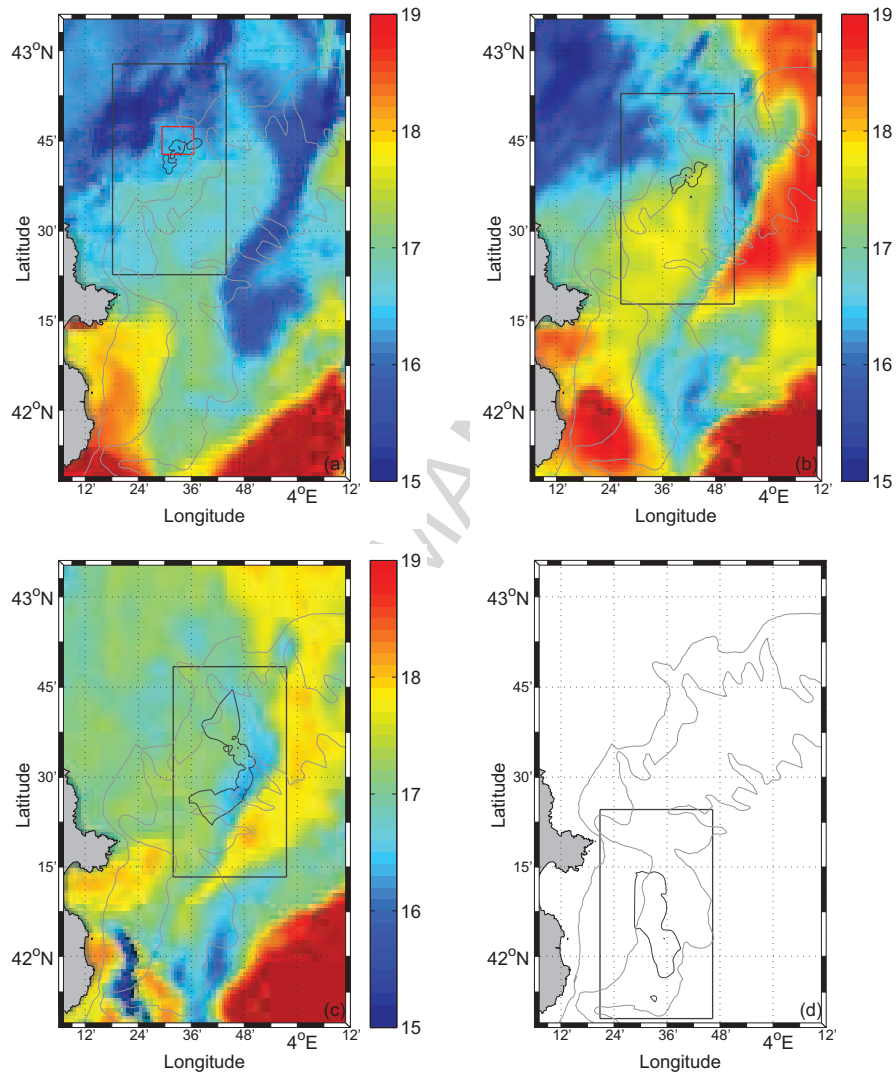


Figure 4: Pseudo-SST satellite image (data from Météo-France) on September 12 (a), September 14 (b), September 15 (c) and Lagrangian contour lines representing the patch area ( $A_{CL}$ ) for each mapping. On September 18 (d), no pseudo-SST satellite image was available due to the cloud coverage, therefore only Lagrangian contour lines are represented. The small red square (a) represents the initial area of  $SF_6$  release. The black squares correspond to the areas of Fig. 2 for each mapping. Isobaths at 100, 200 and 1000 m are plotted with thin lines.

320 interface ( $\text{mol m}^{-3}$ ) and  $\alpha$  the dimensionless Ostwald solubility coefficient. In our experiment the patch is supersaturated with respect to the atmosphere. Therefore, the second term can be neglected compared the first one and we can write the boundary condition as:

$$F|_{z=0} = k(C_w) \quad (5)$$

Performing the analysis in a Lagrangian reference frame allows us to neglect 325 the contribution due to the advection term in equation (1). Moreover, the horizontal diffusivity flux terms should be similar or of smaller magnitude than the loss due to gas transfer because the horizontal gradient of  $C$  is small. [55] shows that dropping the horizontal flux terms is necessary for the analysis, and it can be a valid assumption if the samples are taken well within the tracer 330 patch. Then, the evolution of  $C$  confined in the mixed layer can be strongly simplified as by [64] in the following form:

$$\frac{\partial C}{\partial t} = \frac{\partial}{\partial z} F \quad (6)$$

Using equation (3) and equation (5) as boundary conditions, the vertical integral of equation (6) inside the mixed layer (from 0 to  $-z_{mix}$ ) gives:

$$\frac{\partial \bar{C}}{\partial t} = \frac{-kC_w}{z_{mix}} \quad (7)$$

with  $\bar{C}$  the average concentration of  $SF_6$  in the mixed layer.

335 By making the hypothesis that the water is well mixed over the timescale of concentration decrease due to gas exchange (order of a day), we assumed that  $C_w = \bar{C}$ .  $\bar{C}$  can be assimilated to the measured concentration of  $SF_6$  within an 8% error [64]. Then, equation (7) can be time integrated and rearranged to yield:

$$\bar{C} = \bar{C}_0 e^{\frac{-k}{z_{mix}} t} \quad (8)$$

340

In case the  $SF_6$  patch remains all exposed to exchanges with the atmosphere (i.e. no subduction of the upper mixed layer), equation (8) can be expressed as:

$$\bar{M} = \bar{M}_0 e^{\frac{-k}{z_{mix}} t} \quad (9)$$

with  $\bar{M}$  the total amount of moles of  $SF_6$ .

#### 4.1. Parameterizations of the air-sea transfer velocity

345 To model the  $SF_6$  loss with equation (9), five different parameterizations of the air-sea transfer velocity  $k$  can be found in literature. All of them express  $k$  as a function of the wind speed at 10 m above the sea level ( $U_{10}$ ,  $m\ s^{-1}$ ). The proposed parameterizations vary depending on the time scales considered. In this work, we use  $k_{short}$  for parameterizations based on time scales shorter than 1  
350 day (which also assume steady wind conditions), and  $k_{long}$  for parameterizations based on time scales longer than 1 month (which usually use climatological data). In our analysis, we have used hourly  $U_{10}$  measured from the ship (Fig. 5-a).

The first formulation of  $k$  has been derived in a wind-tunnel experiment  
355 by [65] [LM-86 relationship] and then validated by various fields studies. LM-86 relationship is based on short-term winds but involves three sets of values depending on the dynamics regime. These equations propose a piecewise linear parameterization of  $k_{short}$  on wind speed:

$$\begin{cases} k_{short} = 0.17 U_{10} (Sc_{38}/600)^{-2/3} & \text{for } 0\ m\ s^{-1} < U_{10} \leq 3.6\ m\ s^{-1} \\ k_{short} = (2.85 U_{10} - 9.65) (Sc_{38}/600)^{-1/2} & \text{for } 3.6\ m\ s^{-1} < U_{10} \leq 13\ m\ s^{-1} \\ k_{short} = (5.90 U_{10} - 49.3) (Sc_{38}/600)^{-1/2} & \text{for } U_{10} > 13\ m\ s^{-1} \end{cases} \quad (10)$$

where  $Sc_{38}$  is calculated with a linear extrapolation of the Schmidt number for  
360 seawater with salinity of 35 ( $Sc_{35}$ ) and fresh water ( $Sc_0$ ):

$$\begin{cases} Sc_0 = 3255.3 - 217.13 T + 6.8370 T^2 - 0.086070 T^3 \\ Sc_{35} = 3531.6 - 231.40 T + 7.2168 T^2 - 0.090558 T^3 \end{cases} \quad (11)$$

with  $T$  ( $^{\circ}C$ ) the hourly sea surface temperature data measured by the ship thermosalinometer. The coefficients of equation (11) come from the relationship of [66].

A second parametrization was proposed by [67], who used global  $^{14}C$  calculations  
365 to obtain a quadratic dependence of  $k$  on either short-term or long-term

winds (W-92 relationship):

$$\begin{cases} k_{short} = 0.31 U_{10}^2 (Sc_{38}/660)^{-1/2} \\ k_{long} = 0.39 U_{10}^2 (Sc_{38}/660)^{-1/2} \end{cases} \quad (12)$$

More recently, [68] have also developed a quadratic parameterization (Ho-06 relationship) for high short-term wind conditions ( $U_{10} > 15 \text{ m s}^{-1}$ ) in the western Pacific:

$$k_{short} = 0.266 U_{10}^2 (Sc_{38}/660)^{-1/2} \quad (13)$$

370 A dependency of  $k$  on wind speed stronger than a quadratic relationship has been suggested. For instance, [69] suggested a cubic dependency of  $k$  on either short-term or long-term mean winds conditions (W-99 relationship):

$$\begin{cases} k_{short} = 0.0283 U_{10}^3 (Sc_{38}/660)^{-1/2} \\ k_{long} = (1.09 U_{10} - 0.333 U_{10}^2 + 0.078 U_{10}^3) (Sc_{38}/660)^{-1/2} \end{cases} \quad (14)$$

375 Finally, a formulation of  $k$  based on coastal ocean data has been also developed (N-00 relationship, [70]). [70] express the  $k$  vs wind speed relationship for data from the North Sea experiments. These were also combined with the data of two other studies on Georges Bank and on the West Florida Shelf using the same method to cover a wider range of wind speeds. Such multi-tracer experiment study lead to a second-order polynomial relationship for short-term wind conditions:

$$k_{short} = 0.222 U_{10}^2 + 0.333 U_{10} (Sc_{38}/660)^{-1/2} \quad (15)$$

380 Our time scales between two mappings (order of a day) suggest that the relations with short-term wind are likely to be the more appropriate. However, these relations assume steady wind conditions. In our case, the wind speed variability over the time period considered might be important. The average ship wind for the period from September 11 to September 18 is equal to  $13.3 \text{ m s}^{-1}$  from the hourly data (Fig. 5-a) with a standard deviation of  $6.7 \text{ m s}^{-1}$ ,  
385 showing a significant wind speed variability. In order to evaluate the impact of wind variability and asymmetry, following [71], we can derive two “enhancement

factors”:

$$\begin{aligned}\epsilon_2 &= \overline{U_{10}^2} / \overline{U_{10}}^2 \\ \epsilon_3 &= \overline{U_{10}^3} / \overline{U_{10}}^3\end{aligned}\quad (16)$$

390 For each time period and for any given gas exchange-wind speed relationship, these enhancement factors can be used to assess the contribution of nonlinear dependencies in yielding higher or lower air-sea transfer velocities due to highly variable instantaneous winds ( $k_{inst} = k_{obs}/\epsilon$ ) compared to steady ones. The values of  $\epsilon_2$  range from 0.46 (between the release and Mapping 1) to 1.27 (between Mapping 3 and Mapping 4). This implies that, if a quadratic dependency is assumed, the variation of the wind can reduce the gas exchange by 54 % or enhances it by 27 % during these time periods compared with a steady wind. The values of  $\epsilon_3$  range from 0.74 to 1.87 for the same periods, respectively. This indicates that, if a cubic dependency is assumed, the asymmetry of the wind  
400 can reduce the gas exchange by 26 % or enhances it by 87 % compared with a steady wind.

#### 4.2. Applications

We can now evaluate the evolution of the quantity of  $SF_6$  calculated with the proposed parameterizations. The value  $\bar{M}_0$  in equation (9) is the total amount of  
405  $SF_6$  initially added to the surface mixed layer ( $0.89 \pm 0.11 \text{ mol}$ ). The numerical integration of the modeled loss has been performed with a time-step  $\Delta t = 1 \text{ h}$ , as we have used hourly measurements of the wind speed  $U_{10}$  to calculate  $k$ . In this case, the assumption of the  $SF_6$  patch remaining all exposed to exchanges with the atmosphere seems to be reasonable. To compare this modeled loss of  
410  $SF_6$  to *in situ* data, we have estimated the total quantity of  $SF_6$  in moles by integrating the concentration of  $SF_6$  observed at each mapping over the corresponding total patch area and until the depth of the bottom of the mixed layer ( $-z_{mix}$ ).

Only two relationships are applicable to both short and long wind conditions  
415 (equation (12), W-92 relationship and equation (14), W-99 relationship). We

have evaluated the performance of these relationships by comparing the sum of squared residuals ( $RMS$ ), computed as the difference between the observed and the modeled quantity of  $SF_6$ . Moreover, we computed a second estimate of the  $RMS$  in which an estimate of the standard deviation, associated with the error affecting each measure of  $SF_6$  ( $\pm 5\%$ ), is used to “weight” the contribution of each term within the sum. In both cases the minimum  $RMS$  is found for the short-term wind relationships (data not shown). Hence, we can compare the evolution of the quantity of  $SF_6$  only with the five parameterizations based on short-term wind conditions (lines - Fig. 5-b).

The observed atmospheric loss (black squares - Fig. 5-b) is estimated at about  $0.27 \text{ mol d}^{-1}$  between the release and Mapping 1. The calculated evaporation rate suggests that  $\sim 31\%$  of the released  $SF_6$  is lost during this period, due to the observed increase of wind speed (Fig. 5-a). Between Mapping 1 and 2,  $\sim 57\%$  of the initial amount of  $SF_6$  is further lost with a rate of  $0.27 \text{ mol d}^{-1}$  due to the persistent strong winds ( $20\text{-}25 \text{ m s}^{-1}$  wind speed). Between Mapping 2 and 3, as wind speed decreases to  $\sim 4 \text{ m s}^{-1}$ , the atmospheric loss declines to  $0.01 \text{ mol d}^{-1}$ . The temporal evolution of the wind speed (Fig. 5-a) clearly shows the link between the increase of wind and the decrease of total  $SF_6$  within the patch.

The temporal variability of the measured total  $SF_6$  is in good agreement with the empirical curves. Between the release and Mapping 1 (Mapping 3 and Mapping 4), the empirical curves show generally an underestimate (overestimate) of gas exchange. This can be explained by the enhancement factors due to the variance of the wind, which, as shown before, can substantially reduce (increase) the gas exchange. The N-00 relationship is the most accurate relationship for our data, closely followed by the Ho-06 one. The results show that two of the commonly used parameterizations, the piecewise linear relationship of LM-86 and the cubic relationship of W-99, are inconsistent with measurements of gas transfer velocities at high and variable wind speeds for the coastal area of our study. The quadratic relationship of W-92 is better than the previous two.

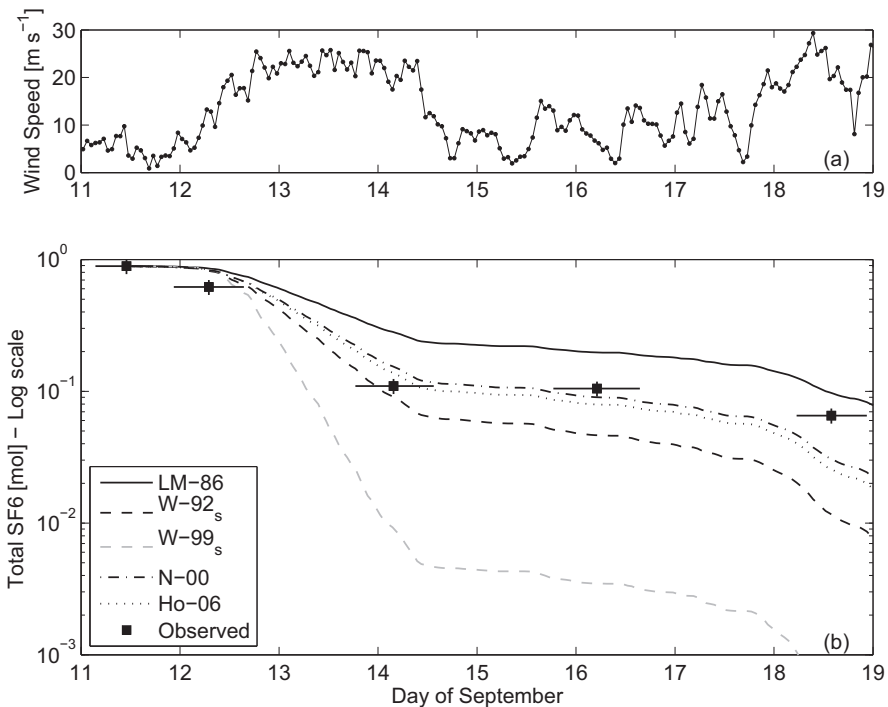


Figure 5: Temporal evolution of (a) the wind speed at 10 m above the sea level ( $U_{10}$ , [ $\text{m s}^{-1}$ ]) as measured from the ship and (b, black squares) observed total  $SF_6$  [mol]. The horizontal and vertical lines over the black squares represent the estimated uncertainties on the calculation of total  $SF_6$  associated to the wind variability, the depth of the mixed layer and the time dependence. They are always calculated but negligible when not visible. The different lines in (b) show the total  $SF_6$  as predicted using the five different parametrization of the air-sea transfer velocity  $k$ . See text for details.

## 5. Lateral diffusivity coefficients

The temporal evolution of the  $SF_6$  patch can be used to quantify the lateral diffusivity coefficient. Various methods have been proposed to obtain this coefficient.

450 We have seen that, between the release and Mapping 2, the sink term representing the atmospheric loss (last term in equation (1)) cannot be neglected. However, after Mapping 2, this sink term becomes very small and linear. Hence,

neglecting it becomes a valid assumption (personal communication, Wanninkhof and Ledwell). The time between the release and Mapping 2 is likely sufficient  
 455 for the complete mixing of  $SF_6$  within the mixed layer (*i.e.* consistent with [55] who suggested a period of 48 h). Therefore, after two days, equation (1) can be reduced to an effective horizontal diffusivity plus a large-scale horizontal strain. As noted in Section 3, the tracer patch does not spread isotropically in the major and minor axis directions. Hence, only the methods based on anisotropic  
 460 spreading are outlined. If we assume a Gaussian distribution, as considered in section 3, the concentration  $C$  as a function of space and time can be expressed as:

$$C = \frac{M}{\sigma_l \sigma_w} e^{-[(x^2/2\sigma_l^2)+(y^2/2\sigma_w^2)]} \quad (17)$$

with  $M$ , the total mass of tracer. Using this relation, the equations of the lengths of the major ( $\sigma_l$ ) and minor ( $\sigma_w$ ) axis of the  $SF_6$  patch can be found by  
 465 multiplying equation (1) by  $x^2$ , or by  $y^2$ , neglecting the atmospheric loss, and integrating over all  $x$ , or over all  $y$  [72, 23, 73].  $\sigma_l$  and  $\sigma_w$  are thus governed by:

$$\frac{d\sigma_l^2}{dt} - 2\gamma\sigma_l^2 = 2K_h \quad (18)$$

$$\frac{d\sigma_w^2}{dt} + 2\gamma\sigma_w^2 = 2K_h \quad (19)$$

These equations can be solved considering different stages of the dispersion of the patch [74]. For a small initial patch,  $(\sigma_l^2, \sigma_w^2) \ll \frac{K_h}{\gamma}$ , the strain effects  
 470 are negligible and equations (18) and (19) can be reduced to the simple Fickian horizontal diffusion model (Fickian model):

$$K_h = \Delta\sigma_l^2/2\Delta t = \Delta\sigma_w^2/2\Delta t \quad (20)$$

where  $\Delta t$  is the difference between the central times of the different mappings. So far, this calculation has been used in areas with different dynamical characteristics than our region of study (*e.g.* interiors of wide shelf sea), usually less  
 475 energetic and/or away from coastal boundaries, shelf break and frontal features [20, 41]. Furthermore, in our case this method cannot be applied due also to the importance of the atmospheric loss term at the beginning of the patch evolution.

For longer times, the strain of the patch cannot be neglected anymore, so that equations (18) and (19) have, respectively, the following solutions:

$$\sigma_l^2 = (\sigma_{l_0}^2 + \frac{K_h}{\gamma})e^{2\gamma t} - \frac{K_h}{\gamma} \quad (21)$$

480

$$\sigma_w^2 = (\sigma_{w_0}^2 - \frac{K_h}{\gamma})e^{-2\gamma t} + \frac{K_h}{\gamma} \quad (22)$$

with  $\sigma_{l_0}$  and  $\sigma_{w_0}$  the initial length of the patch along the directions of the major and minor axes, respectively. This set of equations, known as the diffusion-strain model, allows us to calculate the strain rate ( $\gamma$ ) and the effective horizontal diffusivity ( $K_h$ ) using the values of  $\sigma_l$  and  $\sigma_w$  estimated in Section 3 [e.g. 19].

485

At later stages of the patch dispersion, its width can be hypothesized to be in a near-steady state, i.e. the thinning effect of the strain balances the widening tendency of diffusion (steady state model). This equilibrium can be reached when the time has been long enough so that the transient term, defined in the study of [23] as  $e^{-2\gamma t}$ , is negligible. This balance between the strain rate and the lateral diffusivity is based on the assumption that the currents in the surface ocean are approximately two-dimensional and divergence-free at scales greater than  $\mathcal{O}(1)$  km, conditions typical for regions without intense sub-mesoscale features. In our case, the presence of a front is clearly identified. Nevertheless the assumptions may still hold because of its thermohaline characteristics. Indeed, [63] evidenced the compensated nature of the front, i.e., the horizontal gradient of temperature is balanced by the salinity gradient inducing small horizontal variation of density. Because of that, we can assume the dynamics associated with the front to be dominantly horizontal. At the near-steady state ( $\frac{\partial \sigma_w^2}{\partial t} = 0$ ), the equation for the minor-axis (19) can be written as:

490

$$K_h = \sigma_w^2 \gamma \quad (23)$$

500

In contrast, along the major axis, the length of the patch still increases exponentially at the rate  $\gamma$  and so:

$$\gamma = \frac{\ln(\frac{\sigma_l(t+\Delta t)}{\sigma_l(t)})}{\Delta t} \quad (24)$$

As shown by [28] and [23], this calculation is valid until the horizontal scale of the tracer patch exceeds that of mesoscale eddies. Afterwards the exponential growth stops and the rate of dispersion of the patch can be modeled again  
 505 as a diffusive process (as in equation (20)). In the area, the Rossby radius of deformation for typical stratified late-summer conditions is around 6 km, and mesoscale eddies are usually characterized by diameters between 20 and 30 km [75, 76].

510 In order to quantify the lateral diffusivity coefficients with both the diffusion-strain model and the steady state model, the lengths of the patch defined in section 3 are used. Two distinct conditions are required to apply these dispersal models. Both occurred during the second phase of the temporal evolution of the  $SF_6$  patch discussed in section 3: a) starting at the beginning of Mapping 2,  
 515 the sink term becomes negligible and the exponential growth of the patch is observed (stretching of the patch into a filament) ; b) the horizontal scales of the tracer patch ( $\sigma_w$ ) for all mappings remained within the range typically observed for mesoscale features in the region. Therefore, the rate of dispersion can be adequately evaluated using the two models.

520 For the diffusion-strain model, the initial  $\sigma_{l_0}$  and  $\sigma_{w_0}$  have been defined with the characteristic of Mapping 2 (Table 2). Two  $\sigma_l$  and  $\sigma_w$  have been determined, one for Mapping 3 and one for Mapping 4. We do not consider the case between Mapping 3 and Mapping 4 because the time range between these two mappings was too short. Given these conditions, we can estimate the values  $\gamma$  and  $K_h$   
 525 corresponding to the intersection of the two curves representing, the solutions of equation (21) and equation (22), respectively (Fig. 6-a,b).  $\gamma$  is estimated as  $4.4 \cdot 10^{-6} \text{ s}^{-1}$  and  $K_h$  as  $54.3 \text{ m}^2 \text{ s}^{-1}$  between Mapping 2 and Mapping 3 (Fig. 6-a). Between Mapping 2 and Mapping 4 (Fig. 6-b),  $\gamma$  is estimated as  $2.5 \cdot 10^{-6} \text{ s}^{-1}$  and  $K_h$  as  $23.2 \text{ m}^2 \text{ s}^{-1}$ .

530 Hypothesizing near-steady state conditions, we can also calculate  $\gamma$  and then  $K_h$  with the second model (equations (23) and (24)). Between Mapping 2 and Mapping 3, we find values for  $\gamma$  equal to  $6.7 \cdot 10^{-6} \text{ s}^{-1}$  resulting in a  $K_h$  equal

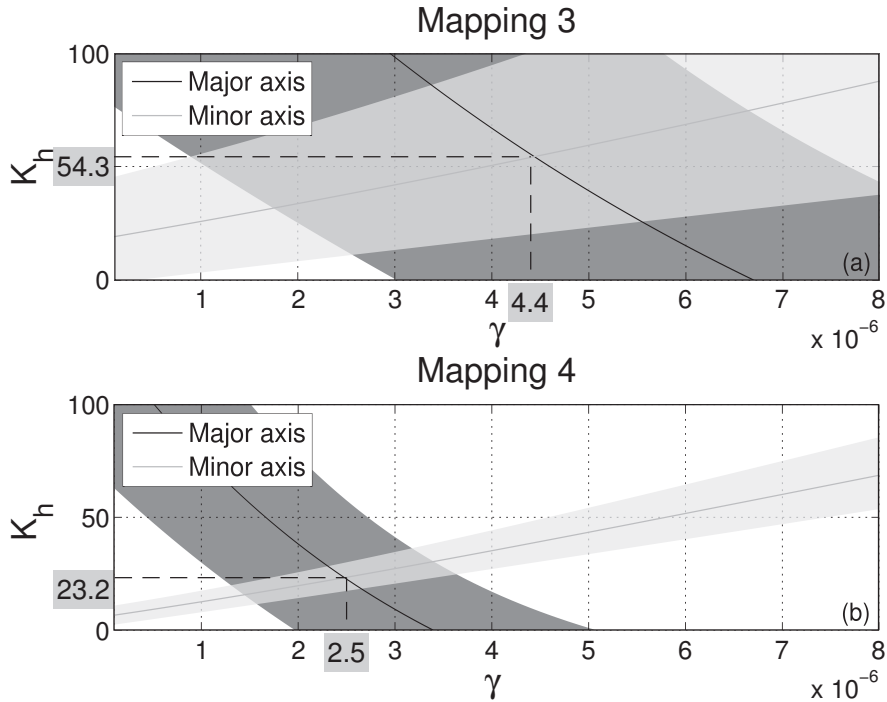


Figure 6: Graphic representation of possible combination of  $\gamma$  [ $s^{-1}$ ] and  $K_h$  [ $m^2 s^{-1}$ ] that could explain the observed growth of the tracer variance from Mapping 2 to Mapping 3 (a), and from Mapping 2 to Mapping 4 (b). The point of intersection of the two curves (equations (21) and (22) in the text) indicates the best estimates of  $\gamma$  and  $K_h$ . The shaded area represents the uncertainties.

to  $70.6 m^2 s^{-1}$ . Between Mapping 2 and Mapping 4,  $\gamma$  is equal to  $3.4 \cdot 10^{-6} s^{-1}$  and  $K_h$  equal to  $29.0 m^2 s^{-1}$ . These different calculations, with associated uncertainties, are summarized in Table 3.

Our results show large uncertainties in the diffusion-strain model results for  $K_h$  as well as large differences between the values of  $K_h$  obtained from the 2 methods between Mapping 2 and Mapping 3. We interpret these discrepancy as an indication that, at this stage, the filament has not yet reached a near-steady state, as also supported by a non negligible transient term. Moreover, the large uncertainties come from the larger errors associated with the Gaussian ellipsoids

fits for Mapping 3.

Between Mapping 2 and Mapping 4, the transient term decreases to 0.15 and the estimate of  $K_h$  is similar for the two models with lower uncertainties. This  
 545 implies that, although the adjustment has not taken place after two days (time interval between Mapping 2 and Mapping 3), it has occurred by Mapping 4, 4.5 days after Mapping 2. Thus the period of adjustment is in the range between 2 and 4.5 days. For this time scale, the transient term becomes negligible and the steady state model can be reasonably used.

Table 3: Estimates of the horizontal diffusivity coefficients and their variation ranges in square brackets with two models with the initial time corresponding to Mapping 2.

	Diffusion-Strain model		Steady state	
	$\gamma$ ( $10^{-6} s^{-1}$ )	$K_h$ ( $m^2 s^{-1}$ )	$\gamma$ ( $10^{-6} s^{-1}$ )	$K_h$ ( $m^2 s^{-1}$ )
Mapping 2 to Mapping 3	4.4 [2.6-5.3]	54.3 [11.1-114.0]	6.7 [6.4 - 7.3]	70.6 [34.7-119.0]
Mapping 2 to Mapping 4	2.5 [1.5-3.2]	23.2 [11.4-36.2]	3.4 [3.0 - 4.0]	29.0 [26.5-32.8]

## 550 6. Discussion and Concluding Remarks

The dynamics of a passive tracer has been studied in a coastal environment during the Latex10 campaign with a Lagrangian approach. Several studies have previously addressed the differences between an Eulerian approach and a Lagrangian one for the calculation of lateral diffusivity coefficient [77]. Generally, the results suggest that an Eulerian approach to calculate lateral diffusivities is most useful for satellite-derived velocity fields or for model outputs. On the other hand, if the measurements and the Lagrangian statistics are adequate, the calculation of lateral diffusivities from drifters trajectories or passive tracer release are the most accurate for *in situ* estimates. Nevertheless, obtaining adequate sampling of the tracer remains a crucial issue in coastal waters.

In our experiment, the tracer patch was followed for seven days, demonstrating the adequacy of the developed LATEXtools for tracer studies in a coastal environment. During and immediately after the release, the weak wind velocity ( $4 \text{ m s}^{-1}$ ) led to an initial slow atmospheric loss. Therefore a good quantification of the total amount of  $SF_6$  initially added to the surface mixed layer ( $0.89 \pm 0.11 \text{ mol}$ ) is possible. We have tested different parameterizations of the ocean-atmosphere gas exchange. The good match between the empirical curves of the atmospheric loss and the total  $SF_6$  mapped (Fig. 5-b) indicates a good coverage of the patch during the various mappings. The largest difference is observed for the total amount of  $SF_6$  measured during Mapping 1. This underestimate of gas exchange in the empirical models can be due to the variance of the wind between the release and Mapping 1. Moreover, during that period, the hypothesis of homogeneity could not be completely respected as the time between the release and Mapping 1 ( $< 48 \text{ h}$ ) is not sufficient for the complete mixing of  $SF_6$ . Despite this underestimation, the formulation of [70], based on data collected in coastal ocean, has proved to be an effective parameterization of gas exchange in our study area.

The area of the tracer patch has been estimated considering two different calculations for the total area of the patch: the Gaussian ellipsoid method or

580 the contour line method. These methods are both based on the assumption of  
a Gaussian distribution of  $SF_6$  concentration within the patch. They provided  
consistent results, with the contour line ones generally lower than the ellipsoid  
ones. This is probably due to the spatial resolution of the sampling that does  
not allow us to find close contour lines for the reference value. Indeed, with this  
585 method, the tracer patch area is calculated summing multiple isolated patches,  
contradicting the Gaussian hypothesis. For this reason, we only summarize the  
temporal evolution of the patch on the basis of the results obtained with the el-  
lipsoid method and we provide estimates of lateral diffusivity coefficients based  
on the lengths of the two axes of the ellipsoids.

590 Two phases can be distinguished in the temporal evolution of the  $SF_6$  patch.  
The first phase corresponds to the time between the release and Mapping 2  
(September 11 - 14, ~67 hours). During this phase, the total patch area initially  
spreads slowly to cover an area of  $71 \pm 4 \text{ km}^2$  with a maximum concentration  
of  $SF_6$  of  $300 \pm 15 \text{ fmol L}^{-1}$ . Furthermore, the patch remains trackable, despite  
595 the sudden increase of wind, starting on September 11 and reaching a maximum  
wind velocity of  $25 \text{ m s}^{-1}$  on September 13. The second phase of the temporal  
evolution of the patch corresponds to the time between Mapping 2 and Map-  
ping 4 (September 14 - 18, ~105 hours). During that phase, the wind velocity  
suddenly decreases then increases again at the end of that period (Fig. 5-a).  
600 We observe that the total patch area increases linearly to eventually cover an  
area of  $377 \pm 9 \text{ km}^2$  (Fig. 3-a). Maximum concentrations of  $SF_6$  inside the total  
patch area are much smaller, with values between  $45\text{-}60 \pm 3 \text{ fmol L}^{-1}$ . In both  
phases, the evolution of the patch geometry (Fig. 3-c) shows a stretching of the  
patch into a filament.

605 Superimposing the distribution of the tracer on the pseudo-SST satellite image  
(Fig. 4) evidences the temporal evolution of the patch relative to the surround-  
ing waters. Pseudo-SST satellite images were available for Mappings 1, 2 and 3  
providing surface information on the dynamical patterns around the patch af-  
fecting its evolution. The presence of a front originating from the convergence of  
610 warmer waters from the Northern Current and colder waters from the shelf has

been discussed in [53]. The presence of the front clearly affects the patch during the second phase of its evolution, inducing its south-westward propagation from the continental shelf of the Gulf of Lion to the Catalan Basin. The presence of a front could affect the divergence-free assumption made for the calculation of the lateral diffusivity coefficients. However, this front has been identified as a compensated front [63], inducing dominantly horizontal dynamics.

In order to evaluate the lateral diffusivity coefficients from the  $SF_6$  patch, we have used the diffusion-strain model and the steady state model. With the diffusion strain model, we obtained a  $\gamma$  of  $2.5 \cdot 10^{-6} \text{ s}^{-1}$  and a  $K_h$  of  $23.2 \text{ m}^2 \text{ s}^{-1}$  between Mapping 2 and Mapping 4, when the atmospheric loss of  $SF_6$  can be neglected. The use of the steady state model can be limited by the near-steady state assumptions, which can be particularly constraining in highly dynamical coastal areas. At the same time, as no processes or structures in the ocean can truly reach a steady-state, the validity of such hypothesis is always relative to the scales of interests. In our case, we showed that an equilibrium could be reached when the time has been sufficiently long for the transient term to become negligible. After a period of adjustment between 2 and 4.5 days, the two models considered in this study converge to similar estimates. Therefore, after such time scale, the order of magnitude of the lateral diffusivity coefficient is not particularly sensitive to the further stretching of the patch.

The horizontal scales characterized by our method are defined by the width ( $2\sigma_w$ ) of the  $SF_6$  patch, equal to  $11.8 \pm 1.4 \text{ km}$ . The observed  $K_h$  of  $23.2 \text{ m}^2 \text{ s}^{-1}$  is in the range of the typical value of  $0.5\text{-}25 \text{ m}^2 \text{ s}^{-1}$  obtained by previous studies which combined estimates of the strain rate with *in situ* measurements of the patch width in high energetic systems [23, 27, 28, 29]. These estimates lie on the canonical diffusion diagram for spatial scales of order 10 km [4].

Our calculation of  $K_h$  includes hypotheses that are generally adopted for analogous experiments: namely, no air-sea loss of  $SF_6$ , and no vertical variations both in horizontal currents (shear) and in vertical diffusivity. The omission of air-sea loss is commonly used in the calculation of lateral diffusivity coefficient as in the studies of [41] and [42]. Moreover it has been shown by [78] that the

omission of air-sea loss and vertical shear in the horizontal currents results in some biases, but that they are small relative to other errors in the estimation of the lateral diffusivity coefficient. At the surface, we have assumed that the  
645 loss to the atmosphere does not affect the analysis. This hypothesis is valid since under the assumption that the  $SF_6$  is homogeneous in the mixed layer the gas transfer velocity is independent of the position in the patch. Concerning the estimate of the exchanges at the bottom of the mixed layer, we observed that the pycnocline, representing the primary barrier to the vertical diffusion of  
650  $SF_6$ , was well marked at about 23 m depth and remained constant during all the experiment.

Since lateral diffusivity coefficients are strongly influenced by local dynamics, comparing them with coefficients calculated for the same region represents a useful test for our estimate. During the Latex10 campaign, the analysis of the  
655 Lagrangian drifters trajectories and transects of surface temperature and salinity across the front allowed the retrieval of an independent series of estimates of  $K_h$  [63]. Their average  $K_h$  is  $4 \text{ m}^2 \text{ s}^{-1}$  with 75 % of the values between 0.5 and  $5 \text{ m}^2 \text{ s}^{-1}$  for horizontal scales in the order of 1 km. In both approaches, two assumptions are made: the large-scale strain field is steady and horizontally  
660 uniform, and the effects of cross-front mixing induced by small scale turbulence can be parameterized by an effective small-scale diffusivity. Although assuming similar hypotheses, the two methods differ by their spatial and temporal scales: the ones associated with the  $K_h$  computed in this study are larger (order of 10 km, and between 2 and 4.5 days) than in [63]. That could explain our larger  
665 values of  $K_h$ .

The lateral diffusivity coefficients have been estimated to a first order from the dynamics of a  $SF_6$  patch in a coastal environment marked by the presence of small-scale dynamical features. The results are consistent with previous studies in open ocean. Thus, with an adapted sampling strategy, passive tracer exper-  
670 iments can be successfully applied also in coastal environments. Such experimental studies are crucial for better understanding the role of lateral diffusivity in coastal areas with important mesoscale and submesoscale activity. They can

provide critical support for further improving the accuracy of regional numerical models used for simulating and predicting the propagation of non-conservative tracers such as nutrients, plankton, and pollutants. Those are key factors in regulating the biological and ecological conditions of coastal region. Improving our understanding of the processes controlling environmental conditions of coastal regions has significant socio-economical implications, and represents a fundamental step towards their sustainable development.

## 7. Acknowledgments

The LATEX project was supported by the programs LEFE/IDAO and LEFE/CYBER of the CNRS/INSU-Institut National des Sciences de l'Univers and by the Region PACA-Provence Alpes Côte d'Azur. Francesco Nencioli acknowledges support from the FP7 Marie Curie Actions of the European Commission, via the Intra-European Fellowship (FP7-PEOPLE-IEF-2011), project Lyapunov Analysis in the COaSTal Environment (LACOSTE-299834). Users can access the data, available at the MIO Laboratory, from the PIs of the LATEX Project, A. A. Petrenko (anne.petrenko@univ-amu.fr) and F. Diaz (frederic.diaz@univ-amu.fr). The SST satellite data were kindly supplied by Météo-France. We are warmly grateful to the crews of the R/V Le Suroît and R/V Téthys II for their assistance. We thank Peggy Rimmelin, Anne Desnues and Marlène Ragot for their invaluable help with the  $SF_6$ . The authors thank Thierry Moutin and David Nerini for precious comments and useful discussions. We thank Dr. Ledwell and Dr. Sundermayer for helpful discussions, encouragement, and for taking the time to respond to our questions. The authors thank Dr. Wanninkhof and Dr. Abernathey, whose comments and suggestions greatly improved the quality of this work. The authors also thank the anonymous reviewers for their constructive remarks. Marion Kersalé was financed by a MENRT Ph.D. Grant.

700 **Appendix A. Analytical system used for the analysis of SF<sub>6</sub>**

The analytical system used for the analysis of SF<sub>6</sub> is based on a continuous flow purge and trap (PT) extraction followed by gas chromatography separation and detection by electron capture detector (GC/ECD). The analytical system is detailed in Fig. A1. We did not use vacuum sparge sample extraction, but  
705 continuous flow of purified nitrogen for extraction of dissolved gases. The water was sampled with a peristaltic pump in a laboratory sink, where surface water circulated after pumping by the ship for thermosalinometer measurements. The ship pump is situated 3 m under the surface. The PT sampling tubing was installed close to the arrival of the water (in the same bucket), in order to both  
710 prevent the water from degassing and minimize the dilution effect in the sink. The water flow entering the degassing system was fixed at 50 ml min<sup>-1</sup>. This flow was adjusted manually in order to keep the degassing system full of water and to insure stability in the extraction efficiency. As the water circulated in the extractor, purified nitrogen (Alpha2 air liquid purified from oxygen, moisture and organic compounds) purged the water at a flow rate of 50 ml min<sup>-1</sup>.  
715 The gas extracted was then desiccated through magnesium perchlorate powder and circulate in 10.47 ml loop. This volume was then injected every 3 min on a cold trap (-100°C ethanol) for three minutes. After 3 min, the trap was isolated (rotation of Va) and immersed in the hot bath (+100°C boiling water).  
720 The trap used was made in a 10 cm, 1/8<sup>e</sup> inch diameter inox tube full with HayesepD phase. This trap allowed the total trapping of SF<sub>6</sub> and CFCs for more than 15 min at -100°C. After 20 s, Vb rotated and the gas trapped were desorbed and injected on a pre-column and on the analytical column for 40 s. After that time, Vb and Va came back to their initial positions. The gas injected was then separated and quantified by the GC/ECD (Perkin Elmer Clarus  
725 500). The precolumn is a PLOT molecular sieve 5A, 1 m long and 0.53 mm diameter. The analytical column is the same but 10 m long. The precolumn protects the column from heavy compounds (VOCs), which could be difficult to elute. The GC oven was fixed at 70°C. The chromatographic analysis was

730 3 min long. The  $SF_6$  extraction efficiency in continuous flow system was calculated and verified by regular analyses of the same water sampled at the same time by sampling ampoules and analyzed by classical PT-GC/ECD technique. The yield of extraction usually varied between 70 and 100 %, depending on the gas and water flow. For one mapping, the flow meter was accidentally partially  
 735 blocked and extraction efficiency dropped to 17 %. As our analytical system could also determine CFC-12 in the same time, our extraction efficiency was also verified for this parameter, which should stay constant in water (function of temperature and salinity). Standardization of the chromatographic system was realized twice a day, with an air standard (NOAA/CMDL standard, 2006  
 740 calibrated air) containing 5.76 pptv of  $SF_6$ . Air standard was injected in loops with various volumes (0.05 ml to 10 ml), in order to obtain a calibration curve. The calibration was linear from 0.2 fmol to more than 35 fmol. Calibration remained very stable throughout the entire campaign.

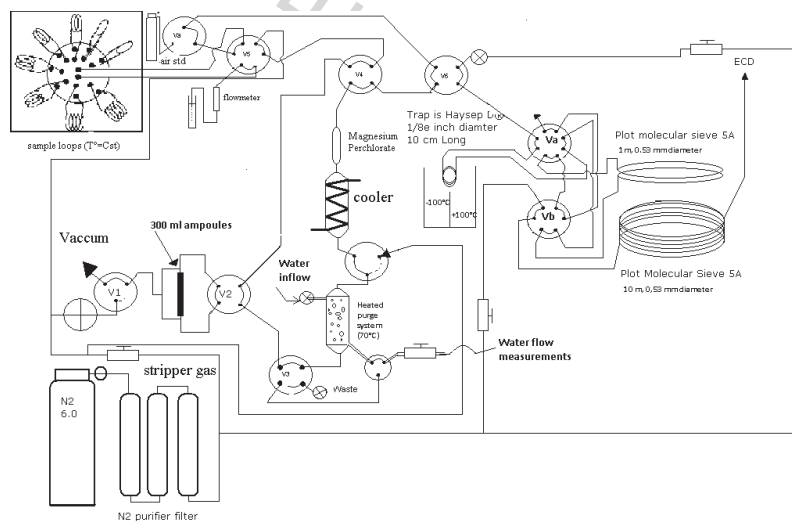


Figure A1: Analytical system used for the analysis of  $SF_6$ , based on continuous flow purge and trap (PT) extraction followed by gas chromatography separation and detection by electron capture detector (GC/ECD).

## References

- 745 [1] L. F. Richardson, Atmospheric diffusion shown on a distance-neighbour graph, in: Proc. R. Soc. London, Series A., Vol. 110, 1926, pp. 709–737.
- [2] L. F. Richardson, H. Stommel, Note on eddy diffusion in the sea, Journal of Meteorology 5 (5) (1948) 238–240.
- [3] H. Stommel, Horizontal diffusion due to oceanic turbulence, J. Mar. Res. 750 8 (3) (1949) 199–225.
- [4] A. Okubo, Oceanic diffusion diagrams, in: Deep sea research and oceanographic abstracts, Vol. 18, Elsevier, 1971, pp. 789–802.
- [5] J. Smagorinsky, General circulation experiments with the primitive equations, i. the basic experiment, Mon. Wea. Rev. 91 (3) (1963) 99–164. 755 doi:10.1175/1520-0493(1963)091<0099:GCEWTP>2.3.CO;2.
- [6] I. James, Advection schemes for shelf sea models, J. Mar. Sys. 8 (1996) 237 – 254. doi:10.1016/0924-7963(96)00008-5.
- [7] B. Fox Kemper, D. Menemenlis, Can Large Eddy Simulation Techniques Improve Mesoscale Rich Ocean Models?, American Geophysical Union, 760 2008, pp. 319–337. doi:10.1029/177GM19.
- [8] A. Bracco, S. Clayton, C. Pasquero, Horizontal advection, diffusion, and plankton spectra at the sea surface, J. Geophys. Res.-Oceans 114 (C2) (2009) n/a–n/a. doi:10.1029/2007JC004671.
- [9] G. Holloway, Estimation of oceanic eddy transports from satellite altimetry, 765 Nature 23 (1986) 243–244.
- [10] R. Ferrari, M. Nikurashin, Suppression of eddy diffusivity across jets in the southern ocean., J. Phys. Oceanogr. 40 (7).
- [11] R. E. Davis, Observing the general circulation with floats, Deep-Sea Res. I 38 (1991) S531–S571.

- 770 [12] J. LaCasce, Statistics from lagrangian observations, *Progress in Oceanography* 77 (1) (2008) 1–29.
- [13] A. C. Haza, T. M. Özgökmen, A. Griffa, A. Molcard, P.-M. Poulain, G. Pegion, Transport properties in small-scale coastal flows: relative dispersion from vhf radar measurements in the gulf of la spezia, *Ocean Dynam.* 60 (4) 775 (2010) 861–882.
- [14] J. C. Ohlmann, J. H. LaCasce, L. Washburn, A. J. Mariano, B. Emery, Relative dispersion observations and trajectory modeling in the santa barbara channel, *J. Geophys. Res.* 117 (C5) (2012) 1978–2012.
- [15] K. Schroeder, J. Chiggiato, A. Haza, A. Griffa, T. Özgökmen, P. Zanasca, 780 A. Molcard, M. Borghini, P.-M. Poulain, R. Gerin, et al., Targeted lagrangian sampling of submesoscale dispersion at a coastal frontal zone, *Geophys. Res. Lett.* 39 (11).
- [16] A. C. Poje, T. M. Özgökmen, B. L. Lipphardt, B. K. Haus, E. H. Ryan, A. C. Haza, G. A. Jacobs, A. Reniers, M. J. Olascoaga, G. Novelli, et al., 785 Submesoscale dispersion in the vicinity of the deepwater horizon spill, *Proceedings of the National Academy of Sciences* 111 (35) (2014) 12693–12698.
- [17] W. J. Emery, R. E. Thomson, *Data analysis methods in physical oceanography*, Elsevier Science, Amsterdam, 2001. doi:10.1016/B978-044450756-3/50000-9.
- 790 [18] W. Geyer, J. Ledwell, Final report: Massachusetts bay dye study, Mass. Water Resour. Auth., Charlestown, Mass. 17 (1994) 13 pp.
- [19] M. A. Sundermeyer, J. R. Ledwell, Lateral dispersion over the continental shelf: Analysis of dye release experiments, *J. Geophys. Res.* 106 (C5) (2001) 9603–9621.
- 795 [20] M. E. Inall, D. Aleynik, C. Neil, Horizontal advection and dispersion in a stratified shelf sea: The role of inertial oscillations, *Prog. Oceanogr.* 117 (2013) 25–36.

- [21] N. Stashchuk, V. Vlasenko, M. E. Inall, D. Aleynik, Horizontal dispersion in shelf seas: High resolution modelling as an aid to sparse sampling, Prog. Oceanogr. doi:10.1016/j.poccean.2014.08.007.
- 800
- [22] R. J. Moniz, D. A. Fong, C. B. Woodson, S. K. Willis, M. T. Stacey, S. G. Monismith, Scale-dependent dispersion within the stratified interior on the shelf of northern monterey bay, J. Phys. Oceanogr. 44 (2013) 1049–1064.
- [23] J. R. Ledwell, A. J. Watson, C. S. Law, Mixing of a tracer in the pycnocline, J. Geophys. Res. 103 (C10) (1998) 21499–21529.
- 805
- [24] D. T. Ho, J. R. Ledwell, W. M. Smethie, Use of  $\text{SF}_6$  for ocean tracer release experiments, Geophys. Res. Lett. 35 (4).
- [25] D. Banyte, M. Visbeck, T. Tanhua, T. Fischer, G. Krahnemann, J. Karstensen, Lateral diffusivity from tracer release experiments in the tropical north atlantic thermocline, J. Geophys. Res. doi:10.1002/jgrc.20211.
- 810
- [26] P. L. Holtermann, L. Umlauf, T. Tanhua, O. Schmale, G. Rehder, J. J. Waniek, The baltic sea tracer release experiment: 1. mixing rates, J. Geophys. Res. 117 (C1). doi:10.1029/2011JC007439.
- [27] T. Stanton, C. Law, A. Watson, Physical evolution of the IronEx-I open ocean tracer patch, Deep-Sea Res. II 45 (6) (1998) 947 – 975. doi:10.1016/S0967-0645(98)00018-6.
- 815
- [28] E. Abraham, C. Law, P. Boyd, S. Lavender, M. Maldonado, A. Bowie, Importance of stirring in the development of an iron-fertilized phytoplankton bloom, Nature 407 (2000) 727–730.
- 820
- [29] A. P. Martin, K. J. Richards, C. S. Law, M. Liddicoat, Horizontal dispersion within an anticyclonic mesoscale eddy, Deep-Sea Res. II 48 (45) (2001) 739 – 755. doi:10.1016/S0967-0645(00)00095-3.

- [30] J. R. Ledwell, A. J. Watson, The Santa-Monica Basin tracer experiment  
825 - A study of diapycnal and isopycnal mixing, *J. Geophys. Res.* 96 (C5)  
(1991) 8695–8718. doi:10.1029/91JC00102.
- [31] R. E. Sonnerup, J. L. Bullister, M. J. Warner, Improved estimates of venti-  
lation rate changes and CO<sub>2</sub> uptake in the Pacific Ocean using chlorofluoro-  
carbons and sulfur hexafluoride, *Journal of Geophysical Research: Oceans*  
830 113 (C12). doi:10.1029/2008JC004864.
- [32] A. Schneider, T. Tanhua, W. Roether, R. Steinfeldt, Changes in ventilation  
of the mediterranean sea during the past 25 yr, *Ocean Science Discussions*  
10 (4) (2013) 1405–1445. doi:10.5194/osd-10-1405-2013.
- [33] T. Tanhua, D. W. Waugh, J. L. Bullister, Estimating changes in ocean  
835 ventilation from early 1990s cfc-12 and late 2000s sf6 measurements, *Geo-  
physical Research Letters* 40 (5) (2013) 927–932.
- [34] C. Law, A. Martin, M. Liddicoat, A. Watson, K. Richards, E. Wood-  
ward, A Lagrangian SF<sub>6</sub> tracer study of an anticyclonic eddy in the  
North Atlantic: patch evolution, vertical mixing and nutrient sup-  
840 ply to the mixed layer, *Deep-Sea Res. II* 48 (4-5) (2001) 705–724.  
doi:10.1016/S0967-0645(00)00112-0.
- [35] J. Martin, K. Coale, K. Johnson, S. Fitzwater, R. Gordon, S. Tanner,  
C. Hunter, V. Elrod, J. Nowicki, T. Coley, et al., Testing the Iron Hy-  
pothesis in Ecosystems of the Equatorial Pacific-Ocean, *Nature* 371 (6493)  
845 (1994) 123–129.
- [36] D. J. Cooper, A. J. Watson, P. D. Nigthingale, Large decrease in ocean-  
surface CO<sub>2</sub> fugacity in response to in situ iron fertilization, *Nature*  
383 (6600) (1996) 511–513.
- [37] D. Tsumune, J. Nishioka, A. Shimamoto, S. Takeda, A. Tsuda,  
850 Physical behavior of the SEEDS iron-fertilized patch by sulphur hex-

- afluoride tracer release, *Prog. Oceanogr.* 64 (2-4) (2005) 111–127.  
doi:10.1016/j.pocean.2005.02.018.
- [38] D. Tsumune, J. Nishioka, A. Shimamoto, Y. W. Watanabe, T. Aramaki,  
Y. Nojiri, S. Takeda, A. Tsuda, T. Tsubono, Physical behaviors of the iron-  
fertilized patch in SEEDS II, *Deep-Sea Res. II* 56 (26) (2009) 2948–2957.  
855 doi:10.1016/j.dsr2.2009.07.004.
- [39] C. Law, W. Crawford, M. Smith, P. Boyd, C. Wong, Y. Nojiri, M. Robert,  
E. Abraham, W. Johnson, V. Forsland, M. Arychuk, Patch evolution and  
the biogeochemical impact of entrainment during an iron fertilisation ex-  
860 periment in the sub-arctic pacific, *Deep-Sea Res. II* 53 (20-22) (2006) 2012  
– 2033. doi:10.1016/j.dsr2.2006.05.028.
- [40] G. Csanady, *Circulation in the coastal ocean*, D.Reidel Publishing Com-  
pany, Kluwer Group, Dordrech, Holland, 1982.
- [41] R. Wanninkhof, G. Hitchcock, W. J. Wiseman, G. Vargo, P. B. Ortner,  
865 W. Asher, D. T. Ho, P. Schlosser, M.-L. Dickson, R. Masserini, et al.,  
Gas exchange, dispersion, and biological productivity on the west florida  
shelf: Results from a lagrangian tracer study, *Geophysical Research Letters*  
24 (14) (1997) 1767–1770.
- [42] M. Yang, S. Archer, B. Blomquist, D. Ho, V. Lance, R. Torres, Lagrangian  
870 evolution of dms during the southern ocean gas exchange experiment: The  
effects of vertical mixing and biological community shift, *J. Geophys. Res.*  
118 (12) (2013) 6774–6790.
- [43] C. Millot, The Gulf of Lions’ hydrodynamics, *Cont. Shelf Res.* 10 (1990)  
885–894. doi:10.1016/0278-4343(90)90065-T.
- [44] C. Albérola, C. Millot, J. Font, On the seasonal and mesoscale variabilities  
875 of the Northern Current during the PRIMO-0 experiment in the western  
Mediterranean Sea, *Oceanol. Acta* 18 (2) (1995) 163–192.

- [45] C. Sammari, C. Millot, L. Prieur, Aspects of the seasonal and mesoscale variabilities of the Northern Current inferred from the PROLIG-2 and PROS-6 experiments, *Deep-Sea Res. I* 42 (6) (1995) 893–917. doi:10.1016/0967-0637(95)00031-Z.
- [46] A. A. Petrenko, Variability of circulation features in the Gulf of Lion NW Mediterranean Sea. Importance of inertial currents, *Oceanol. Acta* 26 (2003) 323–338.
- [47] C. Estournel, X. Durrieu de Madron, P. Marsaleix, F. Auclair, C. Julliand, R. Vehil, Observation and modeling of the winter coastal oceanic circulation in the Gulf of Lion under wind conditions influenced by the continental orography (FETCH experiment), *J. Geophys. Res.* 108 (C3). doi:10.1029/2001JC000825.
- [48] A. A. Petrenko, C. Dufau, C. Estournel, Barotropic eastward currents in the western Gulf of Lion, northwestern Mediterranean Sea, during stratified conditions, *J. Mar. Sys.* 74 (1-2) (2008) 406–428. doi:10.1016/j.jmarsys.2008.03.004.
- [49] P. Conan, C. Millot, Variability of the Northern Current off Marseilles, western Mediterranean Sea, from February to June 1992, *Oceanol. Acta* 18 (2) (1995) 193–205.
- [50] M. M. Flexas, X. Durrieu de Madron, M. A. Garcia, M. Canals, P. Arnau, Flow variability in the Gulf of Lions during the MATER HFF experiment (March-May 1997), *J. Mar. Sys.* 33-34 (2002) 197–214. doi:10.1016/S0924-7963(02)00059-3.
- [51] A. A. Petrenko, Y. Leredde, P. Marsaleix, Circulation in a stratified and wind-forced Gulf of Lions, NW Mediterranean Sea: in situ and modeling data, *Cont. Shelf Res.* 25 (2005) 7–27. doi:10.1016/j.csr.2004.09.004.
- [52] A. Doglioli, F. Nencioli, A. A. Petrenko, J.-L. Fuda, G. Rougier, N. Grima, A software package and hardware tools for in situ experi-

- ments in a Lagrangian reference frame), *J. Atmos. Ocean. Tech.* 30 (8).  
doi:10.1175/JTECH-D-12-00183.1.
- [53] F. Nencioli, F. d'Ovidio, A. M. Doglioli, A. A. Petrenko, Surface coastal  
circulation patterns by in-situ detection of Lagrangian coherent structures,  
910 *Geophys. Res. Lett.* 38 (L17604). doi:10.1029/2011GL048815.
- [54] R. Sugisaki, K. Taki, Simplified analyses of He, Ne, and Ar dissolved in  
natural waters, *Geochemical Journal* 21 (1) (1987) 23–27.
- [55] J. S. Gulliver, B. Erickson, A. J. Zinke, K. S. Shimon, Measurement uncer-  
tainty in gas exchange coefficients, in: M. A. Donelan, W. M. Drennan, E. S.  
915 Saltzman, R. Wanninkhof (Eds.), *Gas Transfer at Water Surfaces*, Ameri-  
can Geophysical Union, 2002, pp. 239–245. doi:10.1029/GM127p0239.
- [56] Z. Y. Hu, A. A. Doglioli, A. M. Petrenko, P. Marsaleix, I. Dekeyser, Numeri-  
cal simulations of eddies in the Gulf of Lion, *Ocean Model.* 28 (4) (2009)  
203 – 208. doi:10.1016/j.ocemod.2009.02.004.
- 920 [57] C. Law, A. Watson, M. Liddicoat, Automated vacuum analysis of sulphur  
hexafluoride in seawater: derivation of the atmospheric trend (19701993)  
and potential as a transient tracer, *Marine Chemistry* 48 (1) (1994) 57 –  
69. doi:10.1016/0304-4203(94)90062-0.
- 925 [58] T. Tanhua, K. Anders Olsson, E. Fogelqvist, A first study of sf6 as a  
transient tracer in the southern ocean, *Deep-Sea Res. II* 51 (22) (2004)  
2683–2699.
- [59] R. Sibson, A brief description of natural neighbor interpolation, in: V. Bar-  
nett (Ed.), *Interpreting Multivariate Data*, John Wiley & Sons, New York,  
USA, 1981, pp. 21–36.
- 930 [60] M. d. Berg, O. Cheong, M. v. Kreveld, M. Overmars, *Computational Geom-  
etry: Algorithms and Applications*, 3rd Edition, Springer-Verlag TELOS,  
Santa Clara, CA, USA, 2008.

- [61] P. Xiu, F. Chai, Modeling the effects of size on patch dynamics of an inert tracer, *Ocean Science* 6 (1).
- 935 [62] J. Lagarias, J. A. Reeds, M. H. Wright, W. P. E., Convergence Properties of the Nelder-Mead Simplex Method in Low Dimensions, *SIAM Journal of Optimization* 9 (1) (1998) 112–147.
- [63] F. Nencioli, F. d’Ovidio, A. Doglioli, A. Petrenko, In situ estimates of submesoscale horizontal eddy diffusivity across an ocean front, *J. Geophys. Res.* 118 (12) (2013) 7066–7080.
- 940 [64] R. Wanninkhof, J. R. Ledwell, W. S. Broecker, M. Hamilton, Gas exchange on mono lake and crowley lake, california, *Journal of Geophysical Research: Oceans* 92 (C13) (1987) 14567–14580. doi:10.1029/JC092iC13p14567.
- [65] P. S. Liss, L. Merlivat, Air-sea gas exchange rates: Introduction and synthesis, in: *The role of air-sea exchange in geochemical cycling*, Springer, 1986, pp. 113–127.
- 945 [66] C. R. Wilke, P. Chang, Correlation of diffusion coefficients in dilute solutions, *AIChE Journal* 1 (2) (1955) 264–270. doi:10.1002/aic.690010222.
- [67] R. Wanninkhof, Relationship between wind-speed and gas-exchange over the ocean, *J. Geophys. Res.* 97 (C5) (1992) 7373–7382. doi:10.1029/92JC00188.
- 950 [68] D. T. Ho, C. S. Law, M. J. Smith, P. Schlosser, M. Harvey, P. Hill, Measurements of air-sea gas exchange at high wind speeds in the southern ocean: Implications for global parameterizations, *Geophys. Res. Lett.* 33 (16).
- [69] R. Wanninkhof, W. R. McGillis, A cubic relationship between air-sea co<sub>2</sub> exchange and wind speed, *Geophysical Research Letters* 26 (13) (1999) 1889–1892.
- 955 [70] P. D. Nightingale, G. Malin, C. S. Law, A. J. Watson, P. S. Liss, M. I. Liddicoat, J. Boutin, R. C. Upstill-Goddard, In situ evaluation of air-sea gas

- 960 exchange parameterizations using novel conservative and volatile tracers,  
Global Biogeochemical Cycles 14 (1) (2000) 373–387.
- [71] R. Wanninkhof, K. F. Sullivan, Z. Top, Air-sea gas transfer in the southern  
ocean, *J. Geophys. Res.* 109 (C8) (2004) 1978–2012.
- [72] A. Townsend, The diffusion of heat spots in isotropic turbulence, *Proceed-*  
965 *ings of the Royal Society of London. Series A. Mathematical and Physical*  
*Sciences* 209 (1098) (1951) 418–430.
- [73] M. A. Sundermeyer, J. F. Price, Lateral mixing and the north atlantic  
tracer release experiment: Observations and numerical simulations of la-  
grangian particles and a passive tracer, *J. Geophys. Res.* 103 (C10) (1998)  
970 21481–21497. doi:10.1029/98JC01999.
- [74] C. Garrett, On the initial streakiness of a dispersing tracer in two-and three-  
dimensional turbulence, *Dyn. Atmos. Oceans* 7 (4) (1983) 265–277.
- [75] Z. Y. Hu, A. A. Petrenko, A. M. Doglioli, I. Dekeyser, Study of mesoscale  
anticyclonic eddy in the western part of the Gulf of Lion, *J. Mar. Sys.* 88  
975 (2011) 3–11. doi:10.1016/j.jmarsys.2011.02.008.
- [76] M. Kersalé, A. M. Doglioli, A. A. Petrenko, I. Dekeyser, F. Nencioli, Phys-  
ical characteristics and dynamics of the coastal latex09 eddy derived from  
in situ data and numerical modeling, *J. Geophys. Res.* 118 (2013) 1–11.  
doi:10.1029/2012JC008229.
- 980 [77] A. Klocker, R. Ferrari, J. H. Lacasce, S. T. Merrifield, Reconciling float-  
based and tracer-based estimates of lateral diffusivities, *J. Mar. Sys.* 70 (4)  
(2012) 569–602.
- [78] C. S. Law, E. R. Abraham, A. J. Watson, M. I. Liddicoat, Vertical eddy  
diffusion and nutrient supply to the surface mixed layer of the antarctic cir-  
985 cumpolar current, *J. Geophys. Res.* 108 (C8). doi:10.1029/2002JC001604.

Dispersion of a patch of the tracer sulfur hexafluoride (SF<sub>6</sub>) in coastal waters

Quantification of gas exchange from the ocean to the atmosphere

Calculation of the local strain rate and the lateral diffusivity coefficient

Application of a steady state model after a period of adjustment (2 and 4.5 days)

ACCEPTED MANUSCRIPT